remote sensing

MDPI

Article

A Bayesian Source Model for the 2022 Mw6.6 Luding Earthquake, Sichuan Province, China, Constrained by GPS and InSAR Observations

Guangyu Xu [1,2], Xiwei Xu [3,*], Yaning Yi [1], Yangmao Wen [4], Longxiang Sun [4], Qixin Wang [1] and Xiaoqiong Lei [1]

[1] National Institute of Natural Hazards, Ministry of Emergency Management of China, Beijing 100085, China; gyxu@ecut.edu.cn (G.X.); yaningyi@ninhm.ac.cn (Y.Y.); qixinwang@ninhm.ac.cn (Q.W.); xiaoqionglei@ninhm.ac.cn (X.L.)
[2] School of Surveying and Geoinformation Engineering, East China University of Technology, Nanchang 330013, China
[3] School of Earth Sciences and Resources, China University of Geosciences (Beijing), Beijing 100083, China
[4] School of Geodesy and Geomatics, Wuhan University, Wuhan 430079, China; ymwen@sgg.whu.edu.cn (Y.W.); lxsundays@whu.edu.cn (L.S.)
* Correspondence: xiweixu@ninhm.ac.cn

Abstract: Until the Mw 6.6 Luding earthquake ruptured the Moxi section of the Xianshuihe fault (XSHF) on 5 September 2022, the region had not experienced an Mw >6 earthquake since instrumental records began. We used Global Positioning System (GPS) and Sentinel-1 interferometric synthetic aperture radar (InSAR) observations to image the coseismic deformation and constrain the location and geometry of the seismogenic fault using a Bayesian method We then present a distributed slip model of the 2022 Mw6.6 Luding earthquake, a left-lateral strike-slip earthquake that occurred on the Moxi section of the Xianshuihe fault in the southwest Sichuan basin, China. Two tracks (T26 and T135) of the InSAR data captured a part of the coseismic surface deformation with the line-of-sight displacements range from ~−0.16 m to ~0.14 m in the ascending track and from ~−0.12 m to ~0.10 m in the descending track. The inverted best-fitting fault model shows a pure sinistral strike-slip motion on a west-dipping fault plane with a strike of 164.3°. We adopt a variational Bayesian approach and account for the uncertainties in the fault geometry to retrieve the distributed slip model. The inverted result shows that the maximum slip of ~1.82 m occurred at a depth of 5.3 km, with the major slip concentrated within depths ranging from 0.9–11 km. The InSAR-determined moment is 1.3×10^{19} Nm, with a shear modulus of 30 GPa, equivalent to Mw 6.7. The published coseismic slip models of the 2022 Luding earthquake show apparent differences despite the use of similar geodetic or seismic observations. These variations underscore the uncertainty associated with routinely performed source inversions and their interpretations for the underlying fault model.

Keywords: Luding earthquake; InSAR; Bayesian inversion; strike-slip fault; coseismic slip distribution

check for updates

Citation: Xu, G.; Xu, X.; Yi, Y.; Wen, Y.; Sun, L.; Wang, Q.; Lei, X. A Bayesian Source Model for the 2022 Mw6.6 Luding Earthquake, Sichuan Province, China, Constrained by GPS and InSAR Observations. *Remote Sens.* **2024**, *16*, 103. https://doi.org/10.3390/rs16010103

Academic Editor: Cristiano Tolomei

Received: 12 November 2023
Revised: 17 December 2023
Accepted: 18 December 2023
Published: 26 December 2023

Copyright: © 2023 by the authors. Licensee MDPI, Basel, Switzerland. This article is an open access article distributed under the terms and conditions of the Creative Commons Attribution (CC BY) license (https://creativecommons.org/licenses/by/4.0/).

1. Introduction

On 5 September 2022, an Mw 6.6 earthquake struck Luding County, Sichuan province, China. As of 17:00 on September 11, the Luding earthquake in Sichuan has killed 93 people, including 55 in Ganzi prefecture and 38 in Ya'an City. Another 25 people are missing, including 9 in Luding County and 16 in Shimian County. Focal mechanism solutions from United States Geological Survey (USGS) indicate that this earthquake is associated with a north–northwest striking left-lateral or west–southwest striking right-lateral fault. The location and sense of motion are consistent with movement on or near the Moxi section of the Xianshuihe fault zone (Figure 1). Almost 22 aftershocks occurred in the period from 5 September 2022 to 5 October 2022, recorded by the China Earthquake Networks Center (CENC). The largest aftershock was the Mw 4.5 earthquake on 7 September 2022.

The Luding earthquake occurred at the east–south margin of the Xianshuihe fault, which is a part of the "eastern Tibet seismic belt" or "N-S tectonic zone" that has experienced a staggering number of M > 7 earthquakes [1]. Since 1700, the XSHF has experienced as many as 17 M > 7 and 29 M > 6.5 earthquakes throughout nearly its entire length along the NW-striking [2,3]. For example, the 1792 M6.75, 1904 M7, and 1981 M6.9 earthquakes on the 45 km long Daofu segment, the 1816 M7.5 and 1973 M7.6 earthquakes on the 90 km long Luhuo segment, and the 1793 M6.7 and 1893 M7.3 earthquakes on the ~62 km long Qianning segment (e.g., [4]). The nearest previous earthquake sequence is the 2014 Kangding Mw5.9 earthquake and its aftershocks, which occurred ~88 km to the northwest of the 2022 Luding earthquake at depths ranging from 5 to 13 km [5].

The 2022 Luding earthquake is the largest earthquake to have occurred near the Moxi section of the Xianshuihe fault, and gives us valuable insight into the poorly understood tectonics of this area. Studying the fault geometry and slip distribution of the Luding earthquake is essential to evaluate regional earthquake hazards, especially because it was near a major city (Kangding). Although several studies have investigated the coseismic slip model of the Luding earthquake using geodetic or seismic data (e.g., [6–8]), the fault slip shows obvious variations both in the shape and coverage area. Meanwhile, some questions about the Luding earthquake remain unresolved, such as how to understand the three aftershocks with normal mechanisms in a strike-slip earthquake sequence, and whether there is any post-seismic deformations accompanied by the intensive aftershocks. Both GPS and InSAR observations recorded the coseismic deformation of the Luding earthquake, but the current research is somewhat limited in the process of combining these two dataset to study the Luding earthquake.

In this study, we use both GPS and Sentinel-1 InSAR data to image the coseismic deformation and present an analysis of the fault location, geometry, and slip distribution of the 2022 Luding earthquake in the framework of Bayesian theory. We then compare our models with the published coseismic slip models to evaluate the impact of model assumptions and employed data sets on the estimated pattern of the coseismic slip. Addtionally, we provide insights on the 2022 Luding earthquake and explore the relationship between coseismic deformation and landslides triggered by the earthquake. Finally, we use the inverted coseismic slip distribution to calculate the Coulomb stress change on the nearby XSH fault.

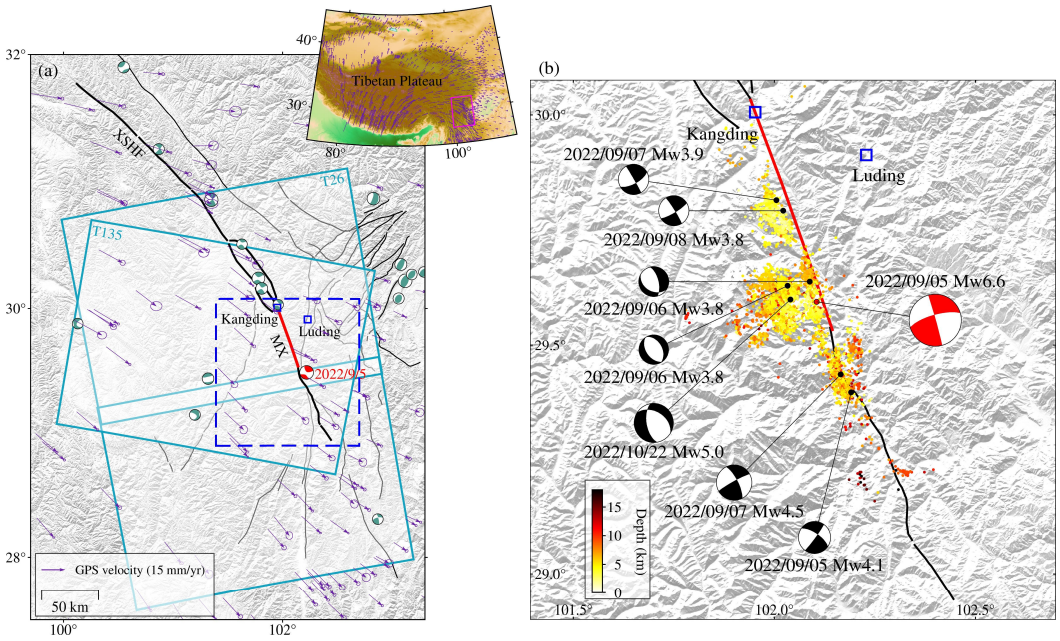


Figure 1. Tectonic setting of the 2022 Luding earthquake. (**a**) Cyan-white beach balls represent focal mechanisms of the historical earthquake since 1990 from GCMT [9]. The red beach ball denotes the

focal mechanism of the 2022 Luding earthquake from GCMT. The dashed blue rectangle shows the area plotted in (**b**). The purple arrows represent GPS velocities [10]. The thin black lines show the active faults. The bold black line denotes the Xianshuihe fault and the red line represents the Moxi section of XSH fault [11]. The light blue polygons are the outlines of areas covered by ascending and descending Sentinel-1 InSAR observations. (**b**) The black beach balls denote focal mechanisms of Mw $\geq$ 3.8 earthquakes in Luding earthquake sequence [12]. The red beach ball denotes the focal mechanism of the 2022 Luding earthquake from USGS. The colored dots represent relocated aftershocks [13].

2. Observations and Coseismic Surface Deformation Field

2.1. InSAR Data

We generated coseismic interferograms from ascending track 26 (26 August 2022 to 19 September 2022) and descending track 135 (2 September 2022 to 14 September 2022) using Sentinel-1 C-band data in the terrain observations with progressive scans in azimuth (TOS) mode (Table 1). We processed the SAR data and generated interferograms with the GAMMA-processing software (version 2023) [14]. All interferograms were generated from the Single Look Complex (SLC) products. The multi-look ratio between the range and azimuth direction was set at 10:2 for Sentinel-1 data. Image co-registration for TOPS mode SAR data is very important and requires extremely high accuracy. To ensure very high co-registration accuracy, a method considering the effects of the scene topography and a spectral diversity method [15] considering the interferometric phase of the burst overlap region were used. After the high-quality co-registration between the TOPS SLC data, the effects of the topography were removed from the interferograms using the 90 m Shuttle Radar Topography Mission (SRTM) digital elevation model (DEM) [16]. The interferograms were then filtered using a power spectrum filter [17] to reduce the effects of phase noise and unwrapped using a minimum-cost flow algorithm [18]. The interferograms were finally geocoded to the WGS84 geographic coordinates with 90 m resolution.

Table 1. Sentinel-1 images used in this study.

Satellite	Reference	Secondary	Direction	Track	Perpendicular Baseline (m)	Incident	Azimuth
Sentinel-1	26 August 2022	19 September 2022	Ascending	26	34	42	−10
Sentinel-1	2 September 2022	14 September 2022	Descending	135	50	35	−169

A troposphere delay may also cause phase errors in InSAR measurements. To account for the potential tropospheric delays and residual orbital errors, a linear function among location (x, y), elevation (h) and error phase were estimated with observations away from the deformed areas (e.g., [19,20]). After the correction, the standard deviations of the ascending and descending line-of-sight (LOS) displacements slightly decreased, respectively.

Both interferograms show obvious coseismic deformation, although the near-fault area exhibits interferometric phase-coherence loss, probably due to vegetational cover or large areas of landslides triggered by earthquakes (Figure 2). The ascending interferogram shows two lobes of deformation with a steep E–W fringe gradient towards the western edge of the interferogram, suggesting that this part of the interferogram is close to the causative fault of the earthquake, and a peak-to-trough LOS deformation of ~15 cm (5 fringes). In the descending interferogram, only one lobe of deformation is visible and the peak-to-trough LOS deformation is ~12 cm (4 fringes). In addition, another three concentric fringes can also be identified in the descending interferogram, which covers an area further to the east of the mapped fault. The InSAR observations all show the largest amplitudes west of the Moxi section of XSHF, suggesting that the fault is slightly dipping westward, as confirmed by the relocated aftershocks [13]. We also performed pixel-offset tracking analysis on both ascending and descending tracks of Sentinel-1 images using the offset

tracking method integrated into InSAR Scientific Computing Environment (ISCE) software (version 2022) [21]. The resulting surface displacements have lower precision and higher noise than LOS observations, but provide useful information near the fault, where LOS observations are mainly decorrelated. (Figure S1). The results of pixel-offset tracking do not show significant surface deformation near the Moxi fault trace (Figure S1), suggesting that the fault slip may not reach the surface.

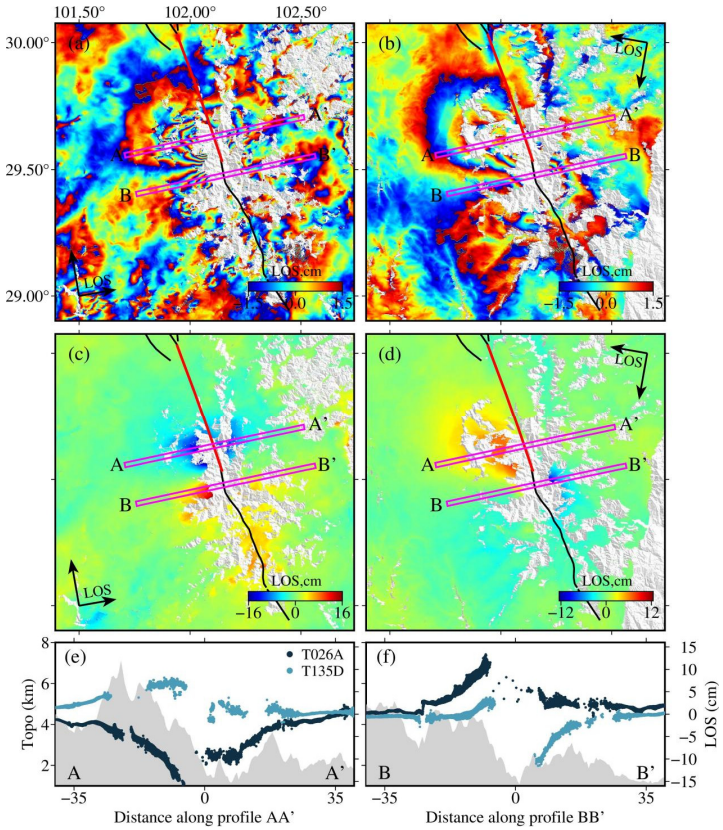


Figure 2. Coseismic InSAR data of the 2022 Luding earthquake. (**a**,**b**) Interferogram of ascending 26 and descending 135, unwrapped and then re-wrapped such that adjacent fringes differ by 3 cm LOS displacement.; (**c**,**d**) LOS displacement of ascending 26 and descending 135; (**e**,**f**) LOS displacements along the two profiles (AA' and BB') shown in (**c**,**d**).

2.2. The Coseismic Displacement of GPS and Strong Motion Data

Coseismic offsets for the Luding earthquake derived from 71 continuous GPS data and 3 strong motion data have been already described in [6] (Figure S2). Henceforth, we refer to these three strong motion sites as GPS sites, as we also utilize the static coseismic deformation obtained from these stations. The complex coseismic deformation pattern highlights a general NNW–SSE-oriented strike-slip mechanism, which is consistent with the deformation field depicted by the InSAR observations. Generally, the GPS coseismic displacements exhibit a typical left-lateral deformation pattern. Sites located east of the fault move towards the north, while sites located west of the fault move towards the south. Sites to the northwest and southeast move toward the fault, while sites to the northeast and southwest move away from the fault (Figure S2). The site closest to the Moxi fault is the strong motion station (51LDJ), about 11 km east of the fault, which measured the largest horizontal displacements (10.8 $\pm$ 0.4 cm). The site ls22, located about 42 km west of the Moxi fault, measured 1.5 $\pm$ 0.1 cm horizontal displacement, which is the largest among the sites west of the fault. [6] did not provide the vertical component given that most of the stations have a low signal-to-noise ratio. Large areas in the near field of the fault lack any GPS data, especially SW of the fault, which weakens the ability to constrain the fault geometry and slip distribution.

2.3. The Comparison between Coseismic InSAR and GPS Offsets

We compared the InSAR coseismic LOS displacement with independent GPS observations to validate the agreement between the two independent observations for the ground deformation of the 2022 Luding earthquake. We only used the GPS sites that have sufficient InSAR observations nearby. The horizontal GPS coseismic offsets were projected to LOS. We compared the GPS-derived LOS displacements with InSAR LOS displacements using the mean of all pixels within 500 m of each GPS station (Figure 3). We confirmed that a good agreement exists between the ascending and descending InSAR and GPS offsets with a large number of sites near the red dashed line (Figure 3). There are some sites for which the InSAR LOS displacements differ by more than 2 mm from the GPS LOS displacements (sites 47, 28 and 72 in Figure 3a and sites 13 and 10 in Figure 3b). Although these sites are all located very close to the black dashed lines, suggesting that the differences between the InSAR LOS and GPS-derived LOS displacements are within acceptable limits, we should still pay attention to the InSAR observations at these locations.

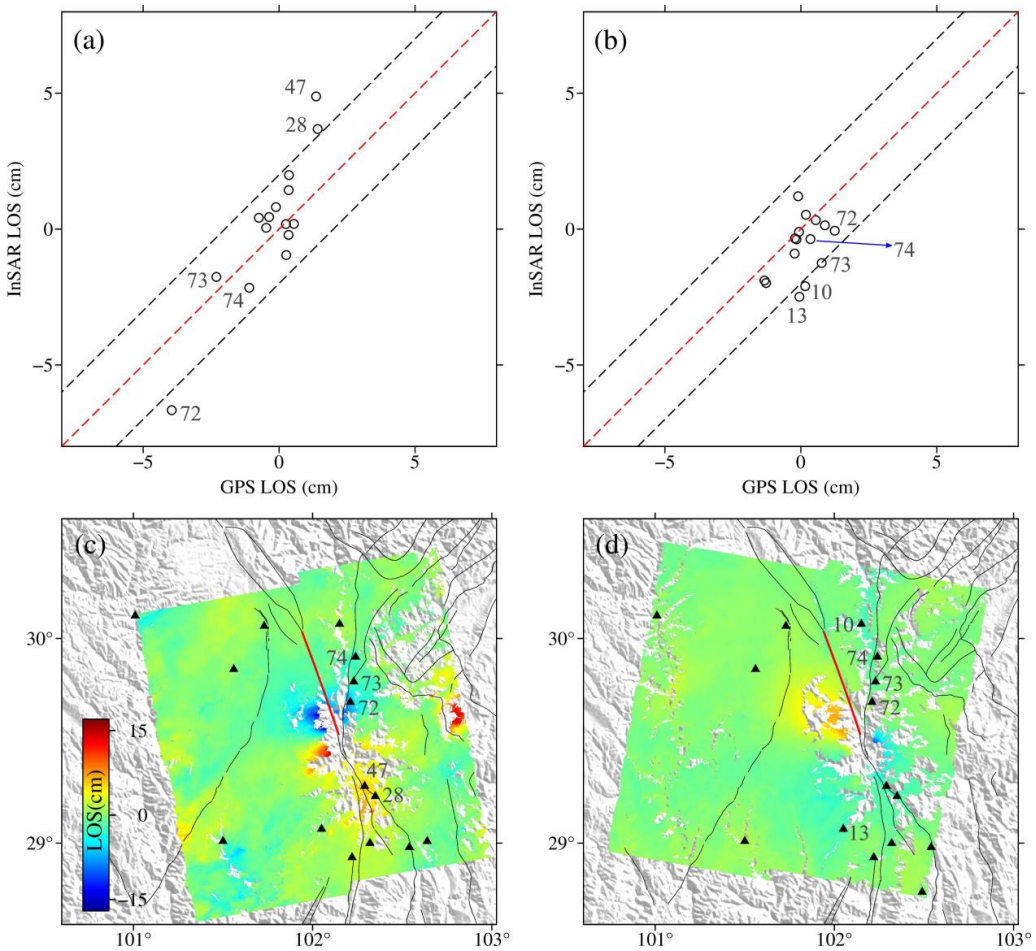


Figure 3. Comparison between InSAR LOS data at the locations of the GPS sites and GPS data projected to LOS from horizontal components. (**a**) Ascending track InSAR LOS versus GPS LOS. (**b**) Descending track InSAR LOS versus GPS LOS. The red dashed line represents perfect agreement and the black dashed lines show a deviation of 2 mm. (**c**) Ascending InSAR LOS map. (**d**) Descending InSAR LOS map. The black triangles denote GPS sites.

2.4. The Three-Dimension Coseismic Deformation of the 2022 Luding Earthquake

To investigate the pattern of coseismic deformation and strain release along the fault, we inverted the three-dimension coseismic deformation of the 2022 Luding earthquake combined with the InSAR and GPS observations. The vertical components of the GPS offsets are not available; therefore, the decomposed vertical component from the InSAR

data is crucial information. For each pixel where information from both ascending and descending tracks is available, Equation (1) is utilized to estimate the east–west and vertical components of the three-dimension coseismic deformation [22].

$$[U_n \sin\Phi - U_e \cos\Phi]\sin\lambda + U_u \cos\lambda + \delta_{los} = d_{los} \quad (1)$$

where ϕ is the azimuth of the satellite heading vector, λ is the radar incidence angle at the reflection point, and δ_{los} is the measurement error. U_e, U_n and U_u denote the east, north, and vertical components of surface displacement field, respectively.

Equation (1) contains three unknowns (U_e, U_n and U_u), but we only have two input InSAR LOS displacements (ascending and descending track InSAR data). In this case, we notice that both the ascending and descending tracks are insensitive to motion in the north–south direction. We therefore use the Kriging interpolation method to obtain a smooth interpolated north–south component (U_n) of the GPS offset in the inversion and solve for the U_e and U_u using the InSAR LOS displacements. The results show that the west side of the Moxi fault mainly moves eastward, with a maximum displacement of ~18 cm (Figure 4a). Since the north–south component of the surface displacement field is interpolated from the north–south component of the GPS offset, the accuracy of the surface displacement in locations without GPS sites cannot be well constrained. Therefore, it is evident that the northward movement of large sections of the western part of the Moxi fault is unreliable, as it contradicts the measurements from two GPS sites located northwest of the fault. Considering the relatively small magnitude (~2 cm) of the northward movement in this area (Figure 4b) and the small proportion (~10%) of the north–south component when projected to the LOS direction, it is unlikely to significantly impact the inversion results of the east–west and vertical components. The east side of the Moxi fault mainly moves northward, which is well constrained by enough GPS sites located northeast of the fault (Figure 4b). At the western side of the southeast end of the Moxi fault, there is a clearly noticeable uplift area with a maximum vertical displacement of ~10 cm. Located approximately 10 km north of the uplift area and west of the Moxi fault, there is a subsidence zone that correlates with the occurrence of numerous relocated aftershocks (Figures 1 and 4).

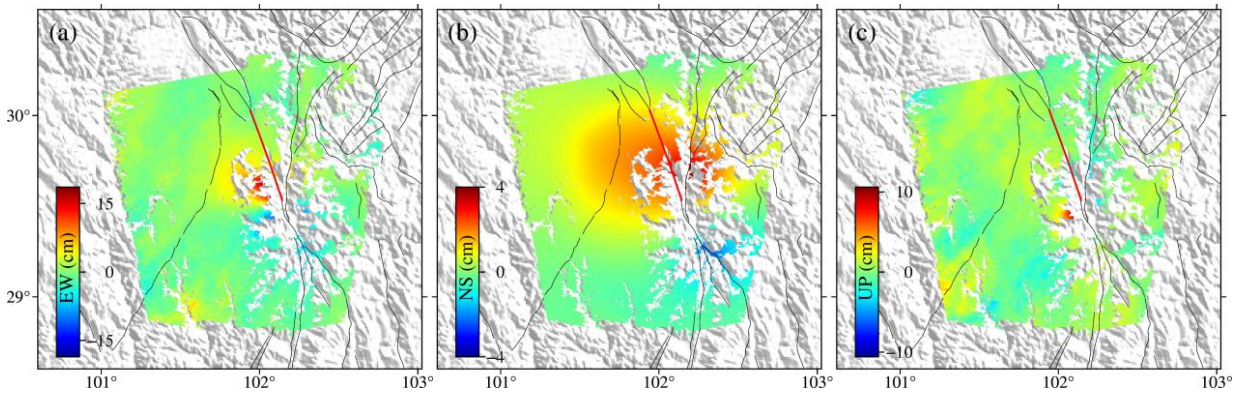


Figure 4. Three-dimension coseismic surface deformation. (**a**–**c**) East, north, and vertical components of the surface displacement field, respectively.

2.5. Aftershock Seismicity

The precisely relocated aftershock distribution shows that aftershocks occur in four major regions [13]: (1) along major XSHF within the ruptured area (area A in Figure 5a); (2) along XSHF but outside the ruptured segment, one to the north (area B in Figure 5a) and another to the south (area D in Figure 5a) of the mainshock rupture area; and (3) to the west of the mainshock rupture area (area C in Figure 5a), which is outside of XSHF. Considering that the aftershock distribution can offer insights into fault geometry, we attempted to determine the strike and dip angles of fault planes based on the aftershock locations in the

four areas, which can serve as a reference. Firstly, we used an L2 norm to fit all located events by a straight line to determine the fault trace of the four areas, respectively. Then, we determined the fault dips by fitting the aftershock locations in profiles perpendicular to the derived fault traces (Figure 5b–m). Due to the approximate circle shape of the aftershock distribution in area C, we made profiles that were perpendicular to and parallel to the derived fault trace (Figure 5d). The results indicate a notable consistency in the derived fault strike orientations of aftershocks in areas A, B and D, all of which align with the XSHF (Figure 5a). The distribution of aftershocks in Region A is most consistent with the southeastward trend of the Moxi Fault. The best-fit line of the aftershock distribution in area A has a strike of 162°. The derived fault trace of aftershocks in area C is nearly perpendicular to the XSHF (Figure 5a). The fault dips derived from the aftershock profiles do not show any regularity due to their relatively discrete distribution in depth (Figure 5f–m). Given the relatively discrete distribution of aftershocks along the depth direction, different perspectives may yield varying results. Among them, the aftershock distribution along the depth direction in profile HH' shows an obvious linear distribution, which suggests that the fault may dip to the east in this area (Figure 5m).

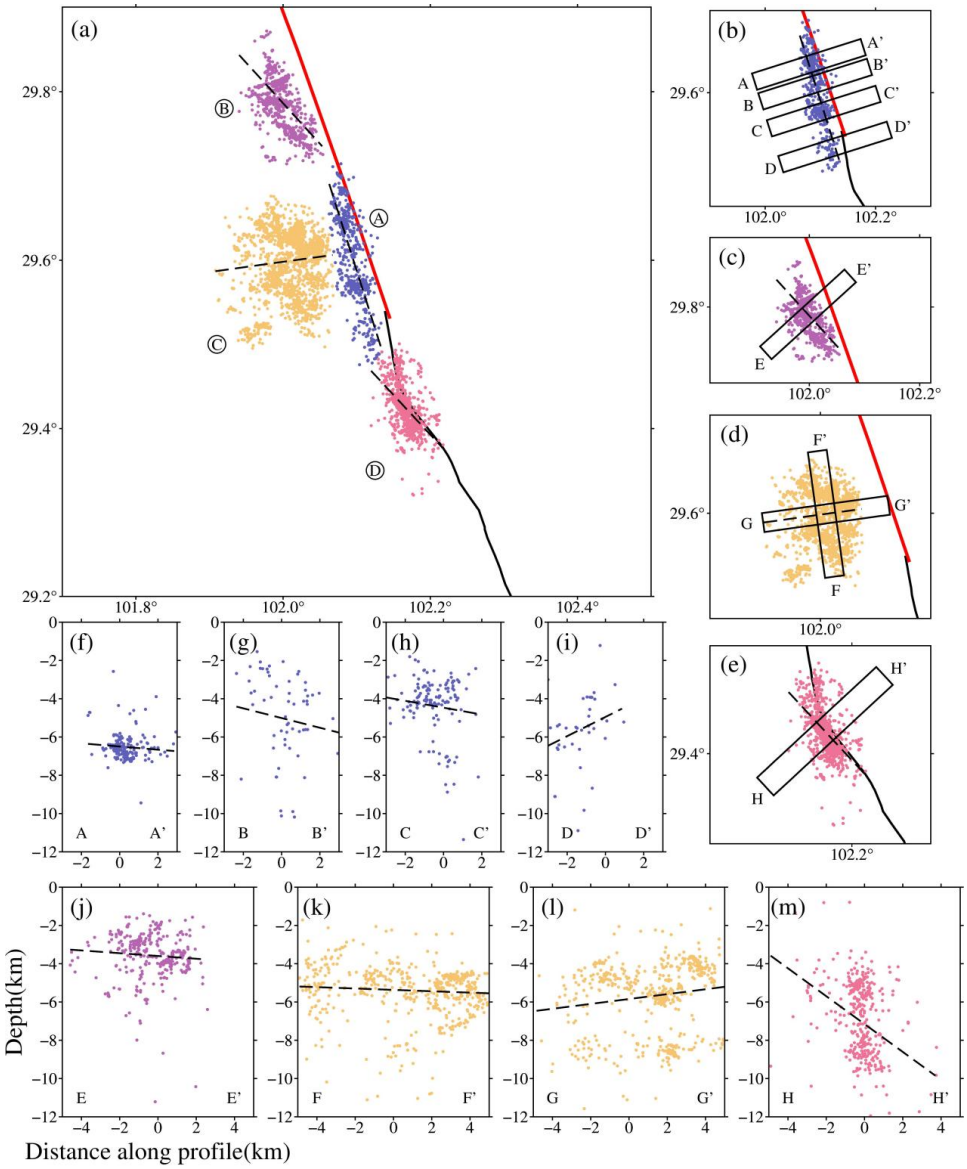


Figure 5. The precisely relocated aftershock distribution. The four different colors of scatter points correspond to the aftershocks in the four mentioned regions A, B, C, and D representing the distribution

of aftershocks. (**a**) Aftershocks in four major regions A, B, C and D. The black dotted lines represent derived fault trace using least squares method. (**b**–**e**) Separate aftershock distribution in four areas. The black rectangles denote profiles (AA', BB', CC', DD', EE', FF', GG' and HH'). (**f**–**m**) Aftershock profiles in depth. The black dotted lines represent fault cross-section derived using least squares method.

3. Modelling

To constrain the location and geometry of the seismogenic fault of the 2022 Luding earthquake, we inverted the InSAR and GPS observation using a two-stage process based on the Bayesian theory: (1) determining the fault parameters with a uniform slip model; (2) estimating the detailed coseismic slip distribution (e.g., [23,24]). To gain a clearer understanding of the role of the GPS and InSAR observations in constraining fault parameters, we conducted separate inversions using GPS alone, InSAR alone and a combination of GPS and InSAR observations.

3.1. The Nonlinear Inversion for Model Parameters

To reduce the computational burden in the inversion, we down-sampled the coseismic InSAR measurements using a resolution-based quadtree method [25]. These down-sampled InSAR data and coseismic GPS offsets are then inverted using a Markov chain Monte Carlo algorithm, which was equipped with Geodetic Bayesian Inversion Software (GBIS) (version 2018) [26] to find the posterior probability distribution of the fault location, size, orientation and slip on a rectangular fault in an elastic half-space [27]. Due to the atmospheric changes between satellite acquisitions that are correlated in space, we calculated a variance–covariance matrix for each InSAR track using the semivariogram method (et al., [28]).

3.2. The Linear Inversion for Slip Distribution

Under the determined location and geometry of the seismogenic fault inverted from the nonlinear inversion, we further extended the fault length and width along the strike and dip directions, respectively. Then, the extended fault plane was subdivided into small fault patches with fixed sizes. Finally, we used a variational Bayesian approach [29] to determine the posteriori probability density function (hereafter PDF) of the slip distribution, data weight ratio and regularization parameters. The variational Bayesian slip distribution inversion method uses an optimization strategy to approximate the posterior PDF of the target, which is detailed in [29]. According to Bayes' theorem, we write the posterior PDF as:

$$p(\mathrm{m}|\,\mathrm{d_{obs}}) \propto p(\mathrm{m})\exp\left[-\frac{1}{2}(\mathrm{d_{obs}}-\mathrm{Gm})^{\mathrm{T}}\mathrm{C_{\chi}^{-1}}(\mathrm{d_{obs}}-\mathrm{Gm})\right] \quad (2)$$

where m is the model vector, p(m) is the prior distribution, $\mathrm{d_{obs}}$ is the data vector, G is the green functions matrix and C_{χ} is the misfit covariance, describing both data and forward prediction uncertainties. We computed Green's functions assuming a homogeneous elastic half-space medium [27].

To weaken the excessive gradient between the slips of the sub-fault patch, we used the Laplacian operator for a priori smoothing. We did not impose any restrictions on the amplitude and direction of the slip to follow the characteristics of the fault rupture reflected in the data itself. Our final solution consists of an ensemble of models that are statistically distributed according to the posterior PDF.

3.3. Accounting for Epistemic Uncertainties

When imaging a slip distribution on a fault, the physics of the forward model is usually assumed to be of minimum complexity to simplify the computation. The uncertainties in fault dip, strike or position, which are the first-order parameters controlling the fault geometry, are assumed to have the largest contribution on the uncertainties of the fault geometry. Accounting for the uncertainties of fault geometry in our forward predictions is crucial, as it corresponds to one of the largest sources of epistemic errors. We thus account

for epistemic uncertainties following the approach developed by the authors of [30] for the fault geometry. The epistemic uncertainties are described by the matrix C_p, which is added to the observation uncertainties matrix C_d to obtain the misfit covariance:

$$C_\chi = C_d + C_p \quad (3)$$

The covariance matrix C_p of epistemic uncertainties is calculated from the sensitivity of Green's functions. Some studies show that fault dip parameters obtained from the nonlinear inversion of the InSAR data are not very accurate. Therefore, it is a common process in linear inversions to determine the fault dip parameters by using a grid search method. In this study, we account for the epistemic uncertainties caused by our poor knowledge of the fault dip and fault position, and integrate them into the Bayesian inversion framework. We assume a 1 km uncertainty in the location of the surface projection of the fault, and a 5° uncertainty in the fault dip (Figure S3), the fault rotating as a whole around its assumed dip.

4. Results

We compared the fault geometry inferred from the separate GPS and InSAR dataset and joint inversions. We found that the optimal uniform slip model determined in all the inversions roughly followed the fault trace of the Moxi fault. These results were not only consistent with each other but also with the independent seismological results (Table 2, Figures 6 and 7, Figures S4–S11). The GPS data supports a steeper dip angle (71.9°) than that inferred from the InSAR data (57.3°). The InSAR data supports a shallower depth (2 km) than that inferred from the GPS data (3 km). The joint inversion of the GPS and InSAR data yields a model with some parameters (fault location, strike, length) lying in between those found from the separate inversions (Table 2). The joint inversion results reveal that the fault is shallower approaching the surface (~0.09 km). The fault width (13.9 km) obtained by the joint inversion is more reasonable than those obtained by GPS inversion alone (2.2 km). The joint inversion further improves the fitness of the InSAR data (RMS = 9.4 mm, Figure 7) compared to the separate InSAR data inversion (RMS = 10.0 mm, Figure S9), while somewhat increasing the misfit of GPS data (RMS = 2.0 mm, Figure 6) compared to the separate GPS data inversion (RMS = 1.3 mm), especially at the 51LDJ site (Figure S6). The convergence of parameters and distribution of joint inversion are more steady and reasonable compared to the separate data inversions (Figures S4, S5, S7, S8, S10 and S11). Most importantly, the joint inversion improves the stability of the inversion parameter results compared to individual data inversion (Table 2). The optimal uniform fault model, determined from the joint inversion of the GPS and InSAR data, reveals a strike of 164° and a dip of 74° to the west. The rupture is estimated to be 19 km long and 14 km wide, with a depth ranging from 0.09 km to 13.45 km, and a left-lateral slip of 1.09 m. The geodetic moment magnitude of the 2022 Luding earthquake model is Mw 6.6, assuming a shear modulus of 30 GPa.

Table 2. Source parameters of 2022 Luding earthquake.

Source	Lon (°)	Lat (°)	Depth (km)	Strike (°)	Dip (°)	Rake (°)	Length (km)	Width (km)	Slip (m)	M0 (10^{19})	Mw	Data
USGS	102.236	29.679	12	254/345	73/88	178/17	-	-	-	1.158	6.6	seismic data
GCMT	102.24	29.50	18.0	164/73	78/83	7/167	-	-	-	1.2	6.7	seismic data
[7]	102.104	29.533	6.10	167.37	73.66	3.3	21.78	10.98	-		6.56	InSAR(Ascending + Descending)
[6]	-	-	-	162,-	80,79	-	70,-	20,-	-	-	6.67, 6.30	GPS + InSAR(Descending)
[8]	102.086	29.589	9.5	163	80	-	50	25	1.5	1.12	6.63	GPS + InSAR(Descending) + seismic data
[13]	102.086	29.589	9.3	166	86	-	39	21	-	-	-	seismic data
[31]	-	-	6.0	161	86	-	-	-	-	-	6.5	GPS
Uniform slip model 1	102.133 [−0.68/0.75km]	29.548 [−0.39/0.48km]	2.89 [−2.47/1.48]	163.22 [−2.16/1.95]	71.87 [−13.10/16.59]	7.00	27.88 [−7.17/3.43]	2.21 [−0.96/5.44]	4.59	0.85	6.59	GPS
Uniform slip model 2	102.153 [−1.04/0.43km]	29.510 [−0.52/0.79km]	1.97 [−1.90/1.47]	173.94 [−5.40/2.49]	57.27 [−8.11/3.55]	14.83	17.01 [−0.88/0.89]	6.55 [−4.06/2.90]	1.97	0.66	6.51	InSAR (Ascending + Descending)
Uniform slip model 3	102.147 [−1.05/0.43km]	29.53 [−0.52/0.79]	0.09 [−0.08/0.38]	164.33 [−0.72/0.76]	73.62 [−2.53/2.61]	−0.13	18.74 [−0.84/1.42]	13.92 [−1.80/0.95]	1.09	0.85	6.59	GPS + InSAR (Ascending + Descending)

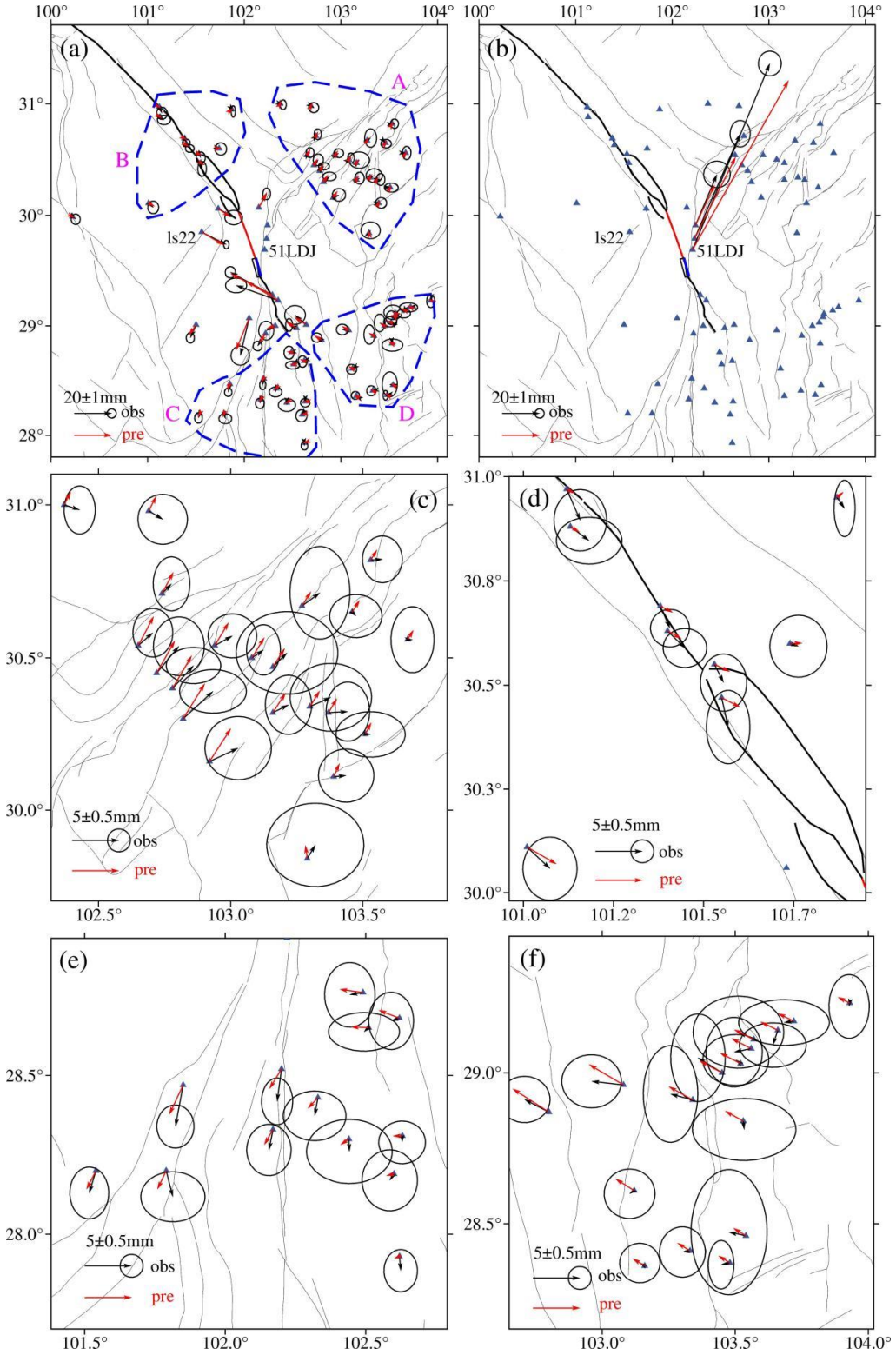


Figure 6. GPS-fitting results of uniform slip model inverted with joint GPS and InSAR data. (**a**) The black arrows show horizontal displacements. (**b**) The black arrows show static horizontal displacements of three strong motion sites. The red arrows denote model predictions. The blue line represents surface projection of uniform slip model. The thin black lines show the active faults. The bold black line denotes the Xianshuihe fault and the red line represents the Moxi section of XSHF [11]. The dashed blue lines outline the areas zoomed in (**c**–**f**).

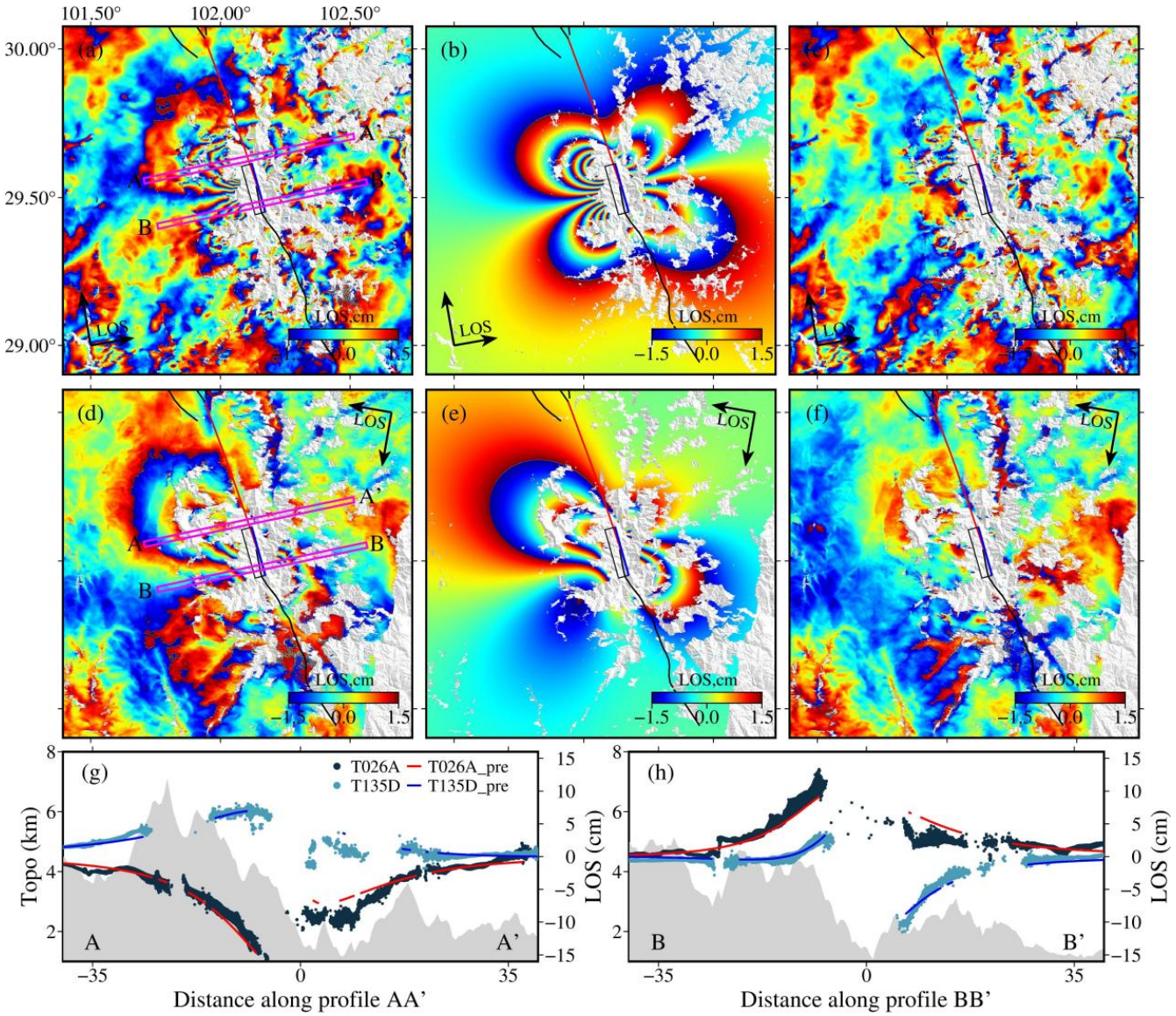


Figure 7. Inversion result of uniform slip model with joint GPS and InSAR data. (**a**,**d**) InSAR observations of ascending track 026 and descending track 135. (**b**,**e**) Model prediction for ascending track 026 and descending track 135. (**c**,**f**) Residuals for ascending track 026 and descending track 135. The black line in (**a**–**f**) represents surface projection of uniform slip model. (**g**,**h**) Fitting result of profile AA' and BB'.

Figures 8 and 9 show the simulated GPS offsets, interferograms and residuals from our best distributed slip model. The optimal distributed slip model shows an elliptical-shape slip distribution with a maximum slip of 1.82 m at a depth of ~5.3 km (Figure 10). The rupture fault is dominated by sinistral strike-slip motion. The total released geodetic moment magnitude is approximately 6.7, which is in agreement with GCMT and USGS results. The main slip area is distributed at a depth of 0.9–11 km (Figure 10). We found that the coseismic deformation of GPS and ascending and descending InSAR data can fit quite well using a single-segment fault, which gives an RMS of about 1.5 mm and 9 mm for InSAR data, respectively.

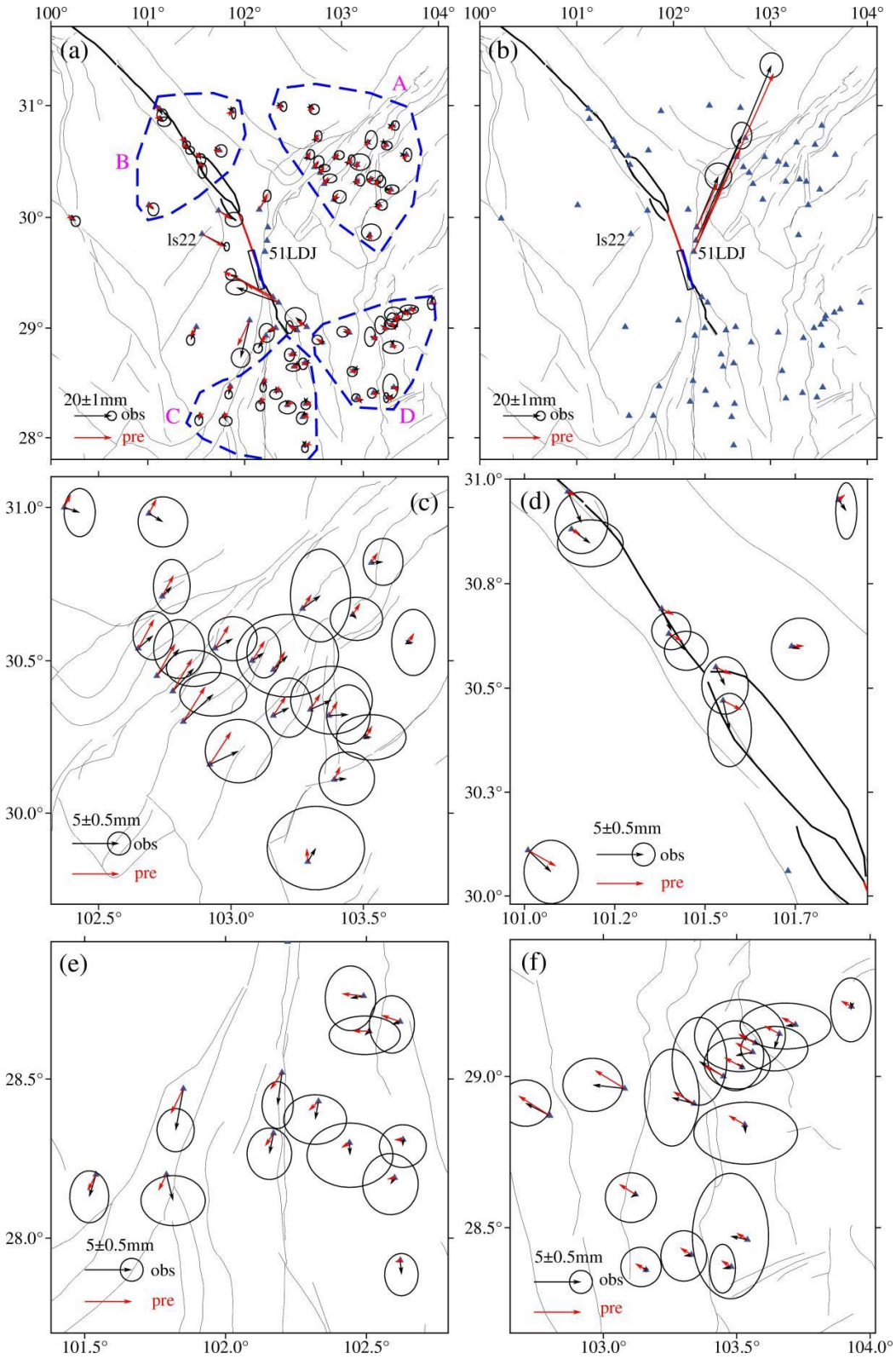


Figure 8. GPS fitting results of optimal distributed slip model inverted with joint GPS and InSAR data. (**a**) The black arrows show horizontal displacements. (**b**) The black arrows show static horizontal displacements of three strong motion sites. The red arrows denote model predictions. The blue line represents surface projection of uniform slip model. The thin black lines show the active faults. The bold black line denotes the Xianshuihe fault and the red line represents the Moxi section of XSHF [11]. The dashed blue lines outline the areas zoomed in (**c**–**f**).

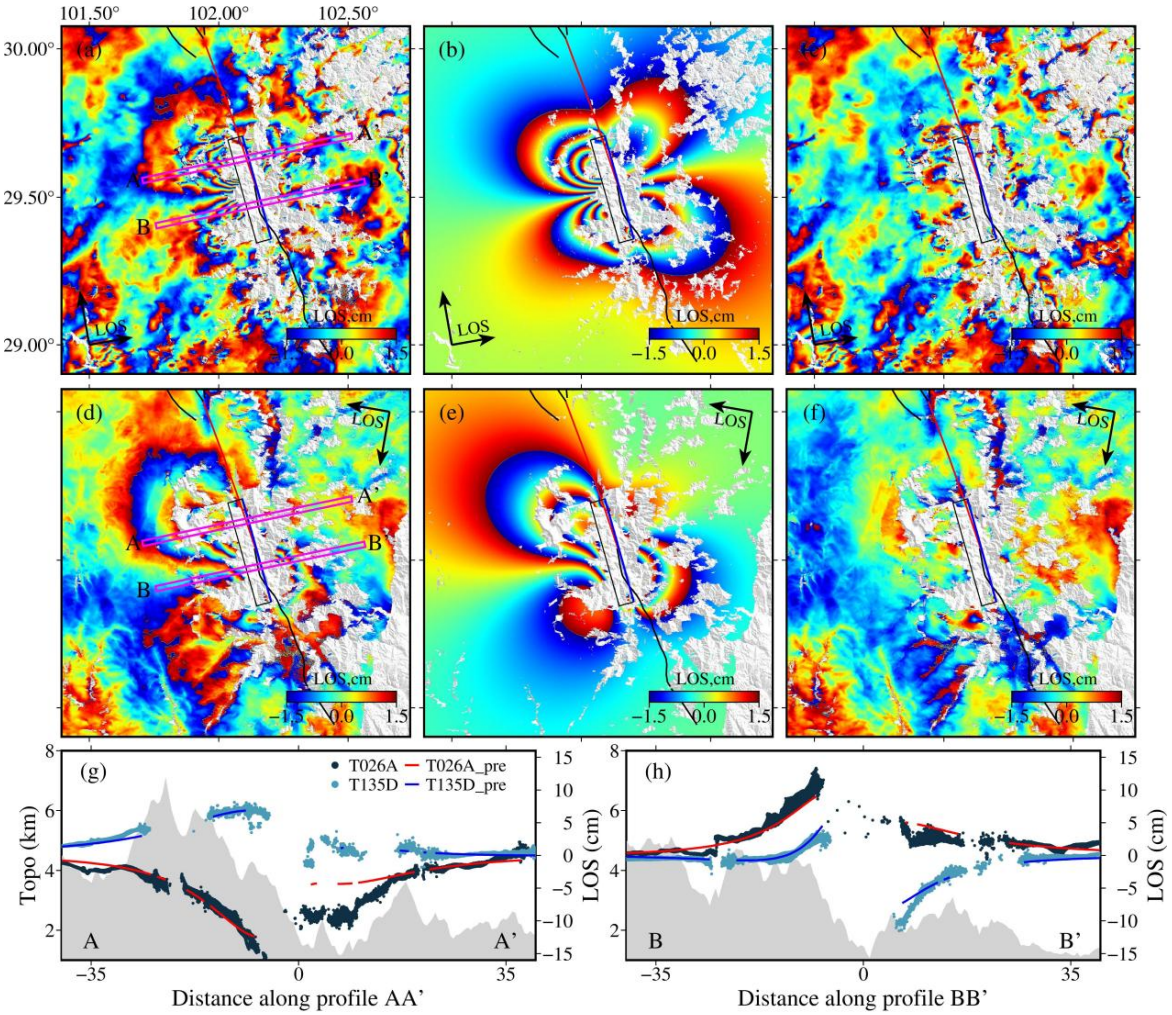


Figure 9. Inversion result of optimal distributed slip model with joint GPS and InSAR data. (**a**,**d**) InSAR observations of ascending track 026 and descending track 135. (**b**,**e**) Model prediction for ascending track 026 and descending track 135. (**c**,**f**) Residuals for ascending track 026 and descending track 135. The black line in (**a**–**f**) represents surface projection of distributed slip model. (**g**,**h**) Fitting result of profile AA′ and BB′.

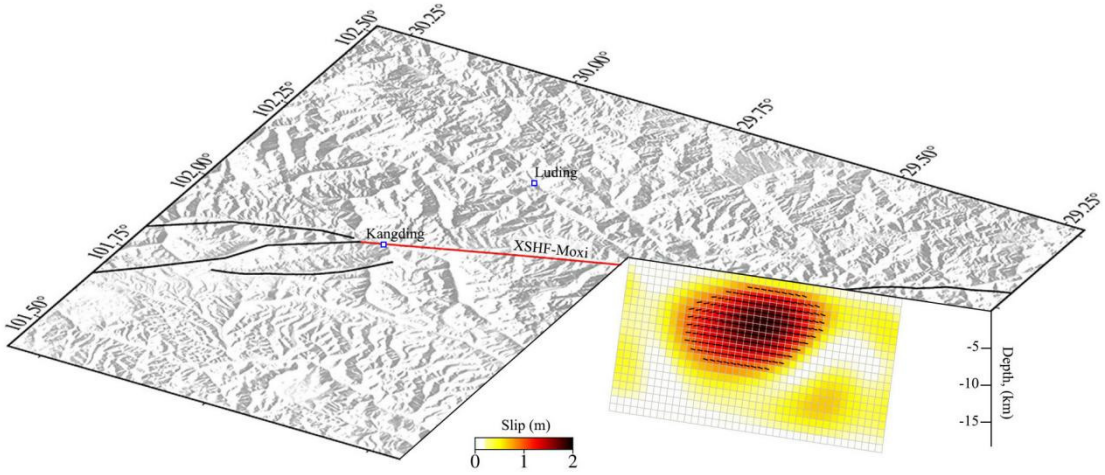


Figure 10. Perspective view on the fault-rupture plane with coseismic slip distribution. Active faults are shown in black and the red line represents the Moxi section of XSHF [11]. The black arrows on the fault plane represent slip vectors with a value larger than 0.8 m.

5. Discussion

5.1. The Comparison of Published Coseismic Slip Models

The coseismic slip model of the 2022 Luding earthquake has already been extensively studied using both geodetic and seismic observations. Several slip models have been published in the literature (e.g., [6–8,13,31–34]). Remarkably, there are substantial differences in terms of both magnitude and slip distributions among many of these models (Figure S12). For example, the maximum slip in the model of [33] was 0.26 m, whereas a peak slip of 2.5 m was obtained in the model of [34]. Moreover, there are notable differences in the spatial distribution of slips among these models. The model of [6] is characterized by a highly heterogeneous slip with three ruptured asperities and a secondary fault perpendicular to the main fault. The models of [13,34] show that the mainshock is mainly featured by two large asperities. The models of [7,8,31–33] show relatively smooth slip variations with only one large asperity. Different models provide different answers regarding whether surface rupture occurred in this earthquake. The models of [6,31,33,34] indicate that the slip reached the surface and extended over a considerable distance, while other models show that the rupture did not reach the surface. The maximum slip reaching the surface is ~1 m in the model of [6], ~1.2 m in [31], ~0.3 m in [33] and ~1 m in [34], and the total length of the slip reaching the surface is ~14 km in the model of [6], ~10 km in [31], ~40 km in [33] and ~10 km in [34] (Figure S12). Here, we should note that the actual situation is that field investigation reports indicate that no significant surface rupture was observed as a result of this earthquake, although they also claim that the surface rupture may be buried by the landslides [35]. Except for the model of [6], the models derived from only geodetic data (i.e., [7,31–33] and the coseismic slip model of this study) generally featured one large asperity.

It is crucial to acknowledge that the resultant slip model is influenced by various factors, including fault geometry, model parameterization, data selection, regularization, and the calculations of Green's functions in the inversion. Therefore, it should be note that this comparison is not intended to determine which model is superior to others [36]. Instead, it is offered to record the fluctuations in these kinds of inversions and offer an understanding of the uncertainty in slip inversions. Nevertheless, we hope that this comparison is informative for assessing how well we can currently resolve the fault structure and coseismic slip model of the Luding earthquake with currently available data.

5.2. Some Thoughts on the 2022 Luding Coseismic Rupture

From the currently published study of the 2022 Luding earthquake, we have discovered that there are still some unresolved issues, such as how many asperities ruptured during this earthquake (one or two asperities); whether there is any post-seismic deformation; and how to understand three aftershocks with normal mechanisms in a strike-slip earthquake sequence. In response to these above questions, we have provided some of our thoughts.

The currently published models of coseismic slip distributions can be mainly classified into two categories: a single asperity [7,8,31–33] and two asperities [13,34]. We should notice that the model of [6] has three asperities, which we will discuss later. The results of two asperities in coseismic slip models are mainly derived from teleseismic data [13,34]. Although the authors of [8] also used the teleseismic data, they inferred only one large slip path in the coseismic slip model. The authors of [13] argued that the authors of [8] may have used a large smoothing factor in their model which resulted in only one asperity. The results of one asperity in coseismic slip models are mainly derived from geodetic data. The coseismic slip model of this study derived from the joint inversion of GPS and InSAR data is also featured with one asperity. Our smoothing factor and coseismic slip distribution were obtained simultaneously using a variational Bayesian method without subjective choice. Therefore, we suggest that if we used geodetic data to constrain the coseismic slip model of the Luding earthquake, one asperity should be a reasonable result. The coseismic slip model with one asperity can fit well with the observation data. The authors of [8] also

used geodetic data in their inversion, and this may be the reason why they only obtained a slip patch even though they used seismic data. Looking back to the model of [6], the authors also used the geodetic data for the inversion and obtained a coseismic slip model with three asperities, which is inconsistent with other models obtained using geodetic data.

The findings of Ref. [13] indicate that some post-seismic processes may have occurred after the Luding earthquake, derived from the relocated aftershock results. To explore whether the aftershock activity was accompanied by the post-seismic deformation, we tried to use InSAR data to image the post-seismic deformation of the Luding earthquake. The post-seismic InSAR observations were generated using the same method as the coseismic results in Section 2. The ascending InSAR of the post-seismic period was from 7 September 2022 to 13 October 2022, and the descending InSAR was from 14 September 2022 to 20 October 2022 (Figure S13). The results showed a large involvement of the post-seismic InSAR observations are decoherence, which also appeared in coseismic interferograms. There are virtually no available post-seismic InSAR observations in the areas corresponding to the two aftershock distribution areas (A and D). The most likely location of post-seismic deformation is near region A, because the location of aftershocks in this region is in most coincidence with the location of the seismogenic fault of the mainshock. The post-seismic InSAR observations in region A are decoherence, and we can not identify post-seismic deformation with some available observations in region A. Although there are enough available post-seismic InSAR observations in regions B and C, no obvious post-seismic deformation signal was observed. We suggest that from the available geodetic observations, there was no surface post-seismic deformation accompanied by the aftershock activity.

The findings of Ref. [12] indicate that there may be a series of SSE/NNW-trending normal faults in the west side of the middle part of the aftershock distribution (between the Gongga Mountain and the Xianshuihe fault zone) that have not been recognized before, which corresponds to three Mw > 3.5 aftershocks with normal mechanisms. Two Mw 3.8 aftershocks occurred one day after the mainshock, which is included in the observation period of the coseismic InSAR. From Figure S14, we can see that the two Mw 3.8 earthquakes with normal focal mechanisms occurred near the northwest side of the seismogenic fault of the mainshock. In this area, the part of the coseismic InSAR observation is incoherent. The ascending and descending track InSAR observations show an opposite deformation, which suggests that the horizontal deformation is dominant here (Figure S14). We did not see clear subsidence signals from normal fault earthquakes in InSAR observations, and we suspect that the small magnitude of these two normal fault earthquakes may not have caused enough surface deformation. Therefore, our geodetic observations can not constrain the fault model of these normal fault earthquakes. Moreover, the aftershock distribution in this region does not show an obvious linear distribution, so it is difficult to constrain the earthquakes of these normal fault mechanisms. The occurrence of normal fault mechanism earthquakes in strike-slip earthquake sequences also exists in some strike-slip events, such as the 1999 Mw 7.1 Hector Mine earthquake [37] and the 2001 Skyros earthquake [38]. Due to the dislocation of strike-slip faults, the positions near one end of the strike-slip faults received the effect of a spreading extension. Therefore, we can see that the normal fault earthquakes mainly occurred on the northwest side of seismogenic fault of the Luding earthquake.

5.3. The Relationship between Coseismic Deformation and Landslides Triggered by the Earthquake

One of the notable aspects associated with the Luding earthquake is the occurrence of extensive landslides across a wide area. Slope stability is related to many factors, such as topography, geology, rainfall, earthquake, etc. Some studies have focused on the analysis of the factors that cause landslides due to the Luding earthquake. Here, we tried to explore the relationship between the coseismic deformation and the landslide areas. The earthquake-triggered landslides were detected and mapped by using on-screen visual interpretation and change-detection methods. Pre-earthquake, Planet images (captured on 7 July and 29 July 2022) and post-earthquake Gaofen-6 images (captured on 10 September 2022) were

therefore collected. The Planet satellite's multispectral band offers a spatial resolution of 3 m, while the Gaofen-6 satellite provides an 8 m spatial resolution for its multispectral band and a 2 m resolution for its panchromatic band. We then carried out image pre-processing operations on the acquired satellite images, including geometric correction, radiometric correction, ortho-rectification, co-registration, image fusion and color enhancement, etc. Finally, a total landslide area of 18.6 km^2 was identified and mapped with the assistance of GIS and ENVI tools.

From Figures 11 and S15, we can see that the landslides triggered by the Luding earthquake are mainly concentrated in the middle of the fault model derived from geodetic observations, which is consistent with the location of the maximum coseismic deformation. Meanwhile, the landslide area is also the main incoherent area of InSAR observations. All detected landslides were located within ~15 km of the earthquake epicenters, with ~50% of the landslide area coinciding with the surface projection of the fault model. A large part of the landslides is located in the main coseismic deformation area, which seems to indicate the influence of coseismic surface deformation on slope stability. We suggest that it is the interaction between the surface deformation and the terrain that causes a large number of landslides triggered by Luding earthquake.

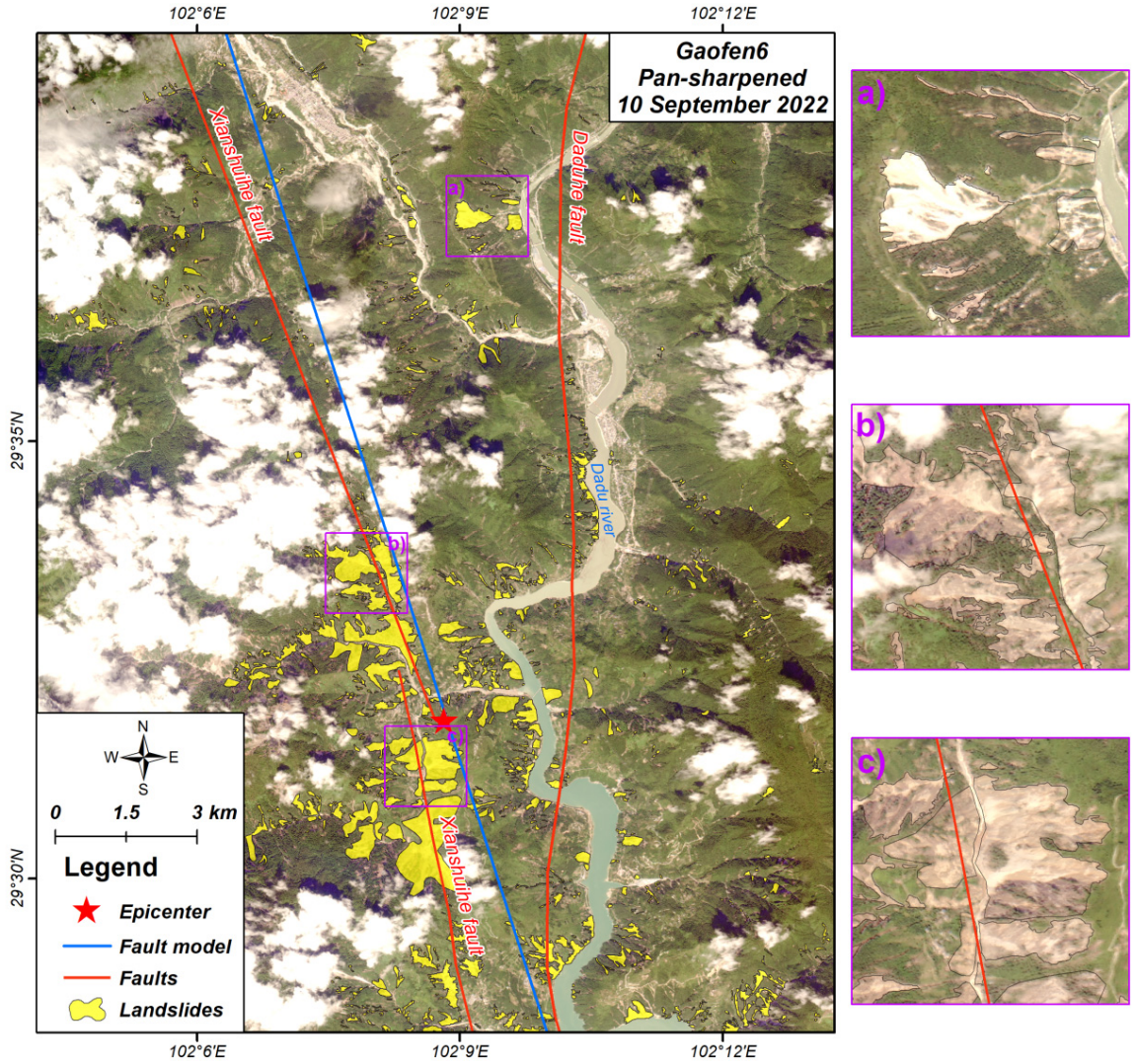


Figure 11. Landslides triggered by 2022 Luding earthquake from Gaofen-6 true color image of the epicentral region. The yellow polygons denote landslide area. The blue line represents surface projection of distributed slip model. The red lines represent active faults [11]. (**a**–**c**) Selected area in purple rectangle boxes in the main figure.

5.4. Coulomb Stress Change

Coulomb stress change calculations strongly depend on the parameterization of the causative coseismic slip model [39]. We used the coseismic slip model of the Luding earthquake derived in our study as the input for calculating the Coulomb stress changes. We estimated both the fault geometry and slip distribution of the earthquake using InSAR, based on data from ascending and descending tracks, as well as coseismic displacements inferred at GPS stations. The effective friction coefficient used in the calculation was 0.4, and the receiving fault strike was consistent with the direction of the mainshock. We calculated the Coulomb stress change at depths of 2, 4, 6 and 8 km using Coulomb 3.3 software [40]. The results show that the regions with positive Coulomb stress change are mainly located at the north and south extremities of the rupture of the Luding earthquake, and in the lobes east and west of the rupture (Figure 12). The relocated aftershocks at different depths are mainly concentrated in areas with positive Coulomb stress changes, which imply that these aftershocks may triggered by stress modifications due to coseismic rupture. The unruptured section and the southeast end of the Moxi fault deserve special attention for their future seismic risk.

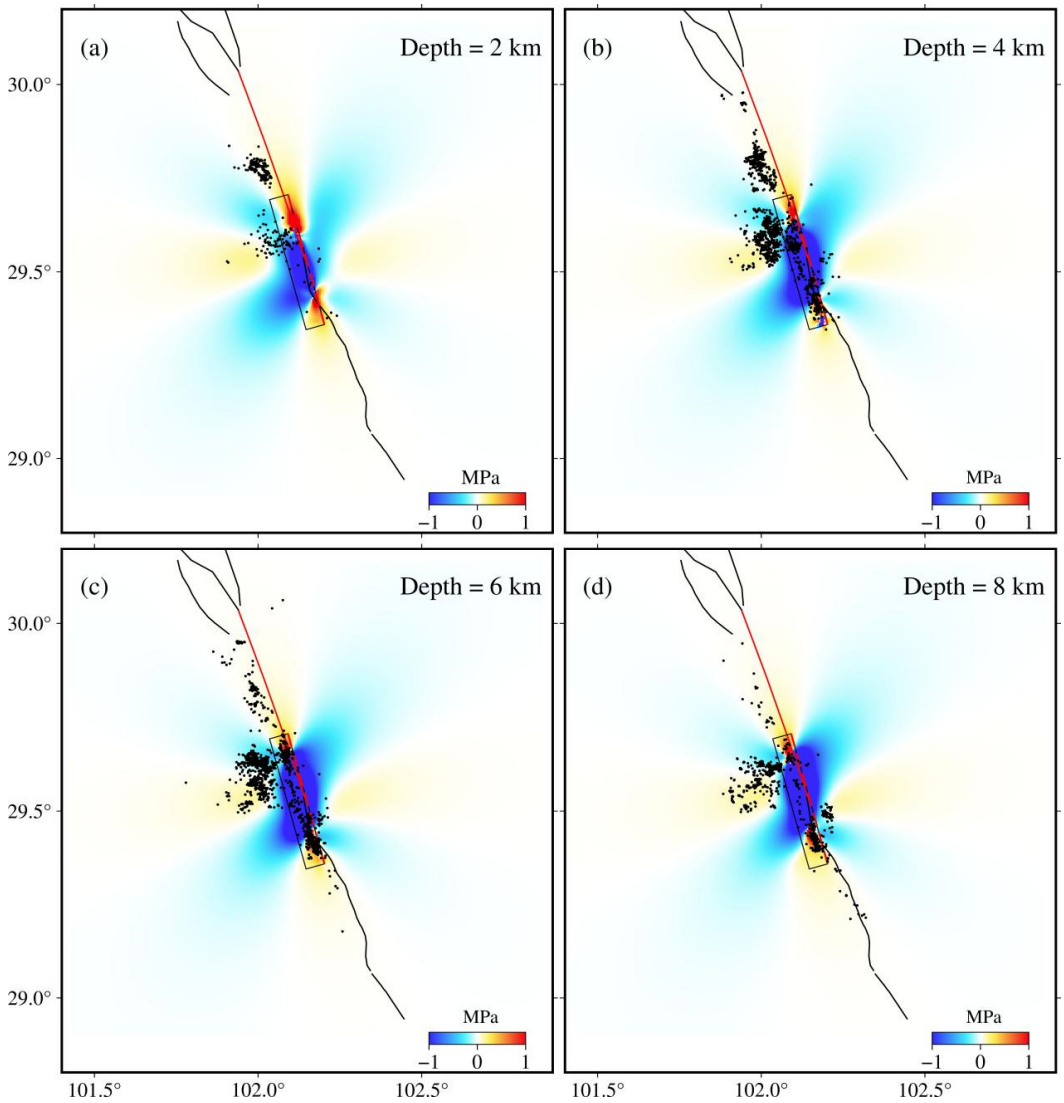


Figure 12. Coseismic Coulomb stress changes induced by the 2022 Luding earthquake at different depth levels. The black dots denote relocated aftershocks between 1 and 3 km depth in (**a**), between 3 and 5 km depth in (**b**), between 5 and 7 km depth in (**c**), and between 7 and 9 km depth in (**d**). The black line in (**a**–**d**) represents surface projection of distributed slip model.

6. Conclusions

Located on the Moxi section of the Xianshuihe fault, the 2022 Luding earthquake is the largest to date ever recorded by instruments. It ruptured a west-dipping fault plane with a strike of 164.3° with a primary sinistral strike-slip motion. Dense aftershocks were distributed in four areas in the west of XSHF, which implies that several faults may have been reactivated during this earthquake sequence, but relocated aftershocks could not constrain the fault geometry of the complex fault system well. Notably, the coulomb stress increased the north and south extremities of the rupture of the Luding earthquake, which is consistent with the location of the aftershocks. The maximum slip of the Luding earthquake was ~1.82 m, at a depth of ~5.3 km. Compared with two major slip patches in fault models obtained from seismic data, the geodetic data support one large slip patch. The post-seismic InSAR data does not capture obvious surface deformation around the aftershock distribution area. Despite the similar data used, the published coseismic slip models of the Luding earthquake show obvious variations, which are likely due to different processing strategies. A Bayesian source model derived from this study will be useful for understanding the real characteristics of the seismogenic fault of the Luding earthquake.

Supplementary Materials: The following supporting information can be downloaded at: https://www.mdpi.com/article/10.3390/rs16010103/s1, Figure S1: Range (a, c) and azimuth (b, d) offset of the ascending track 26 and descending track 135; Figure S2: Static coseismic offsets of 2022 Luding earthquake from GPS and strong motion data [6]; Figure S3: Assumed forward model and associated uncertainties; Figure S4: Parameters convergence of uniform slip model inverted with only GPS data; Figure S5: Distribution of model parameters in the inversion of uniform slip model with only GPS data; Figure S6: Uniform slip model inverted with only GPS data; Figure S7: Parameters convergence of uniform slip model inverted with only InSAR data; Figure S8: Distribution of model parameters in the inversion of uniform slip model with only InSAR data; Figure S9: Inversion result of uniform slip model with only InSAR data; Figure S10: Parameters convergence of uniform slip model inverted with joint GPS and InSAR data; Figure S11: Distribution of model parameters in the inversion of uniform slip mode with joint GPS and InSAR data; Figure S12: Comparison of coseismic slip models for the 2023 Luding earthquake; Figure S13: Wrapped InSAR LOS observations after the earthquake; Figure S14: Wrapped InSAR LOS displacement and focal mechanism result; Figure S15: Wrapped InSAR LOS displacement and landslides area.

Author Contributions: Conceptualization, G.X. and X.X.; methodology, G.X. and Y.Y.; software, G.X.; validation, G.X. and Q.W.; formal analysis, G.X. and Y.W.; investigation, X.L.; resources, Y.W.; data curation, G.X.; writing—original draft preparation, G.X. and L.S.; writing—review and editing, Q.W.; visualization, Y.W.; supervision, X.X.; project administration, X.X.; funding acquisition, X.L. All authors have read and agreed to the published version of the manuscript.

Funding: This research was funded by the National Natural Science Foundation of China (Nos. 41941016, U2139201, 41902217, 41572193, 42104008, 41974004) and the Jiangxi Provincial Natural Science Foundation (20232BAB213075).

Data Availability Statement: The Sentinel-1 data are distributed through ESA data hub.

Acknowledgments: We thank Yijian Zhou for sharing their relocated earthquake catalogs and helpful discussion. The Sentinel-1 data are distributed through ESA data hub. All figures presented in this study are prepared by using the Genetic Mapping Tools (GMT; [41,42]).

Conflicts of Interest: The authors declare no conflict of interest.

References

1. Deng, Q.; Zhang, P.; Ran, Y.; Yang, X.; Min, W.; Chu, Q. Basic characteristics of active tectonics of China. *Sci. China Ser. D Earth Sci.* **2023**, *46*, 356–372. [CrossRef]
2. Allen, C.R.; Zhuoli, L.; Hong, Q.; Xueze, W.; Huawei, Z.; Weishi, H. Field study of a highly active fault zone: The Xianshuihe fault of southwestern China. *Geol. Soc. Am. Bull.* **1991**, *103*, 1178–1199. [CrossRef]
3. Bai, M.; Chevalier, M.; Leloup, P.H.; Li, H.; Pan, J.; Replumaz, A.; Wang, S.; Li, K.; Wu, Q.; Liu, F.; et al. Spatial slip rate distribution along the SE Xianshuihe fault, eastern Tibet, and earthquake hazard assessment. *Tectonics* **2021**, *40*, e2021TC006985. [CrossRef]

4. Wang, H.; Wright, T.J.; Biggs, J. Interseismic slip rate of the northwestern Xianshuihe fault from InSAR data. *Geophys. Res. Lett.* **2009**, *36*, L03302. [CrossRef]
5. Jiang, G.; Wen, Y.; Liu, Y.; Xu, X.; Fang, L.; Chen, G.; Gong, M.; Xu, C. Joint analysis of the 2014 Kangding, southwest China, earthquake sequence with seismicity relocation and InSAR inversion. *Geophys. Res. Lett.* **2015**, *42*, 3273–3281. [CrossRef]
6. Li, Y.; Zhao, D.; Shan, X.; Gao, Z.; Huang, X.; Gong, W. Coseismic Slip Model of the 2022 Mw 6.7 Luding (Tibet) Earthquake: Pre-and Post-Earthquake Interactions with Surrounding Major Faults. *Geophys. Res. Lett.* **2022**, *49*, e2022GL102043. [CrossRef]
7. Han, B.; Liu, Z.; Chen, B.; Li, Z.; Yu, C.; Zhang, Y.; Peng, J. Coseismic deformation and slip distribution of the 2022 Luding Mw 6.6 earthquake revealed by InSAR observations. *Geomat. Inf. Sci. Wuhan Univ.* **2023**, *48*, 36–46, (In Chinese with English abstract).
8. Guo, R.; Li, L.; Zhang, W.; Zhang, Y.; Tang, X.; Dai, K.; Li, Y.; Zhang, L.; Wang, J. Kinematic slip evolution during the 2022 Ms 6.8 Luding, China, earthquake: Compatible with the preseismic locked patch. *Geophys. Res. Lett.* **2023**, *50*, e2023GL103164. [CrossRef]
9. Dziewonski, A.M.; Chou, T.; Woodhouse, J.H. Determination of earthquake source parameters from waveform data for studies of global and regional seismicity. *J. Geophys. Res. Solid Earth* **1981**, *86*, 2825–2852. [CrossRef]
10. Wang, M.; Shen, Z.-K. Present-day crustal deformation of continental China derived from GPS and its tectonic implications. *J. Geophys. Res. Solid Earth* **2020**, *125*, e2019JB018774. [CrossRef]
11. Xu, X.W.; Han, Z.J.; Yang, X.P.; Zhang, S.; Yu, G.; Zhou, B.; Li, F.; Ma, B.; Chen, G.; Ran, Y. *Seismotectonic Map in China and its Adjacent Regions*; Seismological Press: Beijing, China, 2016. (In Chinese)
12. Yi, G.; Long, F.; Liang, M.; Zhao, M.; Zhang, H.; Zhou, R.; Li, Y.; Liu, H.; Wu, P.; Wang, S.; et al. Seismogenic structure of the 5 September 2022 Sichuan Luding MS6.8 earthquake sequence. *Chin. J. Geophys.* **2023**, *66*, 1363–1384, (In Chinese with English abstract).
13. Zhang, L.; Zhou, Y.; Zhang, X.; Zhu, A.; Li, B.; Wang, S.; Liang, S.; Jiang, C.; Wu, J.; Li, Y.; et al. 2022 Mw 6.6 Luding, China, Earthquake: A Strong Continental Event Illuminating the Moxi Seismic Gap. *Seismol. Res. Lett.* **2023**, *94*, 2129–2142. [CrossRef]
14. Wegnüller, U.; Werner, C.; Strozzi, T.; Wiesmann, A.; Frey, O.; Santoro, M. Sentinel-1 Support in the GAMMA Software. *Procedia Comput. Sci.* **2016**, *100*, 1305–1312. [CrossRef]
15. Scheiber, R.; Moreira, A. Coregistration of interferometric SAR images using spectral diversity. *IEEE Trans. Geosci. Remote Sens.* **2000**, *38*, 2179–2191. [CrossRef]
16. Farr, T.G.; Rosen, P.A.; Caro, E.; Crippen, R.; Duren, R.; Hensley, S.; Kobrick, M.; Paller, M.; Rodriguez, E.; Roth, L.; et al. The shuttle radar topography mission. *Rev. Geophys.* **2007**, *45*, RG2004. [CrossRef]
17. Goldstein, R.M.; Werner, C.L. Radar interferogram filtering for geophysical applications. *Geophys. Res. Lett.* **1998**, *25*, 4035–4038. [CrossRef]
18. Chen, C.W.; Zebker, H.A. Network approaches to two-dimensional phase unwrapping: Intractability and two new algorithms. *J. Opt. Soc. Am. A* **2000**, *17*, 401–414. [CrossRef] [PubMed]
19. Wen, Y.; Xu, C.; Liu, Y.; Jiang, G. Deformation and source parameters of the 2015 Mw 6.5 earthquake in Pishan, western China, from Sentinel-1A and ALOS-2 data. *Remote Sens.* **2016**, *8*, 134. [CrossRef]
20. Feng, W.; Samsonov, S.; Almeida, R.; Yassaghi, A.; Li, J.; Qiu, Q.; Li, P.; Zheng, W. Geodetic Constraints of the 2017 Mw7.3 Sarpol Zahab, Iran Earthquake, and Its Implications on the Structure and Mechanics of the Northwest Zagros Thrust-Fold Belt. *Geophys. Res. Lett.* **2018**, *45*, 6853–6861. [CrossRef]
21. Rosen, P.A.; Gurrola, E.; Sacco, G.F.; Zebker, H. The InSAR scientific computing environment. In Proceedings of the EUSAR 2012, 9th European Conference on Synthetic Aperture Radar, Nuremberg, Germany, 23–26 April 2012; pp. 730–733.
22. Fialko, Y.; Simons, M.; Agnew, D. The complete (3-D) surface displacement field in the epicentral area of the 1999MW7.1 Hector Mine Earthquake, California, from space geodetic observations. *Geophys. Res. Lett.* **2001**, *28*, 3063–3066. [CrossRef]
23. Wright, T.J.; Lu, Z.; Wicks, C. Source model for the Mw 6.7, 23 October 2002, Nenana mountain earthquake (Alaska) from InSAR. *Geophys. Res. Lett.* **2003**, *30*, 1974. [CrossRef]
24. Atzori, S.; Hunstad, I.; Chini, M.; Salvi, S.; Tolomei, C.; Bignami, C.; Stramondo, S.; Trasatti, E.; Antonioli, A.; Boschi, E. Finite fault inversion of DInSAR coseismic displacement of the 2009 L'Aquila earthquake (central Italy). *Geophys. Res. Lett.* **2009**, *36*, L15305. [CrossRef]
25. Lohman, R.B.; Simons, M. Some thoughts on the use of InSAR data to constrain models of surface deformation: Noise structure and data downsampling. *Geochem. Geophys. Geosystems* **2005**, *6*, Q01007. [CrossRef]
26. Bagnardi, M.; Hooper, A. Inversion of surface deformation data for rapid estimates of source parameters and uncertainties: A Bayesian approach. *Geochem. Geophys. Geosystems* **2018**, *19*, 2194–2211. [CrossRef]
27. Okada, Y. Surface deformation due to shear and tensile faults in a half-space. *Bull. Seismol. Soc. Am.* **1985**, *75*, 1135–1154. [CrossRef]
28. Parsons, B.; Wright, T.; Rowe, P.; Andrews, J.; Jackson, J.; Walker, R.; Khatib, M.; Talebian, M.; Bergman, E.; Engdahl, E.R. The 1994 Sefidabeh (eastern Iran) earthquakes revisited: New evidence from satellite radar interferometry and carbonate dating about the growth of an active fold above a blind thrust fault. *Geophys. J. Int.* **2006**, *164*, 202–217. [CrossRef]
29. Sun, L.; Wang, L.; Xu, G.; Wu, Q. A new method of variational Bayesian slip distribution inversion. *J. Geod.* **2023**, *97*, 10. [CrossRef]
30. Ragon, T.; Sladen, A.; Simons, M. Accounting for uncertain fault geometry in earthquake source inversions–I: Theory and simplified application. *Geophys. J. Int.* **2018**, *214*, 1174–1190. [CrossRef]
31. Liang, H.; Wu, Y.; Shao, Z.; Li, J.; Li, Y.; Yi, S.; Yang, F.; Zhuang, W.; Wang, H.; Zhan, W.; et al. Coseismic slip and deformation mode of the 2022 Mw 6.5 Luding earthquake determined by GPS observation. *Tectonophysics* **2023**, *865*, 230042. [CrossRef]

32. Peng, W.; Huang, X.; Wang, Z. Focal Mechanism and Regional Fault Activity Analysis of 2022 Luding Strong Earthquake Constraint by InSAR and Its Inversion. *Remote Sens.* **2023**, *15*, 3753. [CrossRef]
33. Wu, W.; Meng, G.; Liu, T.; Wei, C.; Wei, W. Coseismic displacement field and slip distribution of the 2022 Luding M6. 8 earthquake derived from GNSS observations. *Chin. J. Geophys.* **2023**, *66*, 2306–2321, (In Chinese with English abstract).
34. Zhao, X.; Xiao, Z.; Wang, W.; Li, J.; Zhao, M.; Chen, S.; Tang, L. Fine seismogenic fault structures and complex rupture characteristics of the 2022 M6.8 Luding, Sichuan earthquake sequence revealed by deep learning and waveform modeling. *Geophys. Res. Lett.* **2023**, *50*, e2023GL102976. [CrossRef]
35. Shan, X.; Li, Y.; Gao, Z.; Hua, J.; Huang, X.; Gong, W.; Qu, C.; Zhao, D.; Chen, J.; Huang, C.; et al. Coseismic deformation of the 2022 Luding MS6.8 earthquake and seismic potential along adjacent major faults. *Chin. Sci. Bull.* **2022**, *68*, 944–953, (In Chinese with English abstract). [CrossRef]
36. Wang, K.; Dreger, D.S.; Tinti, E.; Bürgmann, R.; Taira, T. Rupture process of the 2019 Ridgecrest, California Mw6.4 foreshock and Mw7.1 earthquake constrained by seismic and geodetic data. *Bull. Seismol. Soc. Am.* **2020**, *110*, 1603–1626. [CrossRef]
37. Hauksson, E.; Jones, L.M.; Hutton, K. The 1999 M w 7.1 Hector Mine, California, earthquake sequence: Complex conjugate strike-slip faulting. *Bull. Seismol. Soc. Am.* **2002**, *92*, 1154–1170. [CrossRef]
38. Karakostas, V.G.; Papadimitriou, E.E.; Karakaisis, G.F.; Papazachos, C.B.; Scordilis, E.M.; Vargemezis, G.; Aidona, E. The 2001 Skyros, Northern Aegean, Greece, earthquake sequence: Off-fault aftershocks, tectonic implications, and seismicity triggering. *Geophys. Res. Lett.* **2003**, *30*, 1012. [CrossRef]
39. Woessner, J.; Jónsson, S.; Sudhaus, H.; Baumann, C. Reliability of Coulomb stress changes inferred from correlated uncertainties of finite-fault source models. *J. Geophys. Res. Solid Earth* **2012**, *117*, B07303. [CrossRef]
40. Toda, S.; Stein, R.S.; Sevilgen, V.; Lin, J. Coulomb 3.3 Graphic-rich deformation and stress-change software for earthquake, tectonic, and volcano research and teaching—User guide. *US Geol. Surv. Open-File Rep.* **2011**, *1060*, 63.
41. Wessel, P.; Smith, W.H. New, improved version of Generic Mapping Tools released. *Eos Trans. Am. Geophys. Union* **1998**, *79*, 579. [CrossRef]
42. Wessel, P.; Luis, J.F.; Uieda, L.; Scharroo, R.; Wobbe, F.; Smith, W.H.; Tian, D. The generic mapping tools version 6. *Geochemistry* **2019**, *20*, 5556–5564. [CrossRef]

Disclaimer/Publisher's Note: The statements, opinions and data contained in all publications are solely those of the individual author(s) and contributor(s) and not of MDPI and/or the editor(s). MDPI and/or the editor(s) disclaim responsibility for any injury to people or property resulting from any ideas, methods, instructions or products referred to in the content.